Check for updates

ADVANCED ENERGY MATERIALS
www.advenergymat.de

Autonomous Control of Ion Migration at α-$FAPbI_3$ Heterointerfaces via Interfacial-Self-Assembled 2D Perovskite

*Jihyun Kim, Ji-Sang Park, Gee Yeong Kim, and William Jo**

Harmonizing homogeneity in charge distribution within metal halide perovskite solar cells is essential for maintaining device quality. The adsorption of ions from perovskites onto the electron transport layer leads to the creation of redistributed space-charge regions (SCR), which facilitate halide segregation and ionic migration, resulting in charge imbalances and diminished extraction capability at the interface. The research examines the intricate interplay between SCRs affecting iodide oxidation and their impact on photovoltaics, uncovering a previously overlooked aspect that the influence of ionic accumulation on electronic charge uniformity. A paradox is identified that electronic charge accumulation at interfaces improves initial open-circuit voltage, however, compromises stability with a collapsed charge distribution. To address this issue, ion conduction is regulated by utilizing a self-assembled 2D perovskite resulting from cationic exchange with a low migration barrier at the buried interface, thereby mitigating halide segregation and charge inhomogeneity. This approach exhibits a power conversion efficiency (PCE) of 24.38% with a fill-factor of 84% and maintains 91.87% of the initial PCE for a duration of 2070 h.

1. Introduction

Formamidinium (FA)-based perovskites, characterized by their superior thermal stability,[1] diminished hydrogen vacancy-induced recombination centers,[2] and mitigated ionic migration[3] in comparison to their methylammonium (MA)-based counterparts, find universal use in highly efficient perovskite solar cells (PSCs). In the configuration of all-perovskite multijunction solar cells, which surpass the Shockley-Queisser efficiency limit of single-junction solar cells, FA is typically employed in both wide-bandgap and narrow-bandgap materials for the top and sub-cells, respectively.[4,5]

However, these halide-based perovskites exhibit dual electronic and ionic conduction, predominantly influenced by iodine vacancies that induce unbalanced local stoichiometric variations.[6,7] This phenomenon leads to the degradation of perovskite materials in narrow-bandgap compositions, as well as phase segregation in wide-bandgap counterparts, thereby compromising charge extraction efficiency at the interface due to heightened non-radiative recombination.[4,8,9] Hence, the necessity to stabilize perovskite devices, especially by precisely controlling the ionic behavior at the interface between charge transport layers and perovskites, emerges as a crucial research frontier that needs to be addressed prior to widespread commercialization.[10–13] Interface engineering strategies have been explored for perovskites to enhance the stability and device performance. These strategies encompass a wide spectrum, from incorporating additives[14] during the precursor synthesis process to implementing interface passivation techniques both above and below the perovskite layer. Despite these endeavor, typical passivation materials for PSCs have been observed to lead to the accumulation of electronic charges at the interfaces and non-uniformities in the bulk, as a major factor in the decline of device performance.[15] Since analysis of the correlation between the heterojunction interface and passivation materials, as well as comprehension their influence on perovskite, remains challenging and ambiguous, elucidating the charge carrier dynamics is essential to uncover the underlying factors.

J. Kim, W. Jo
Department of Physics
Ewha Womans University
Seoul 03760, Republic of Korea
E-mail: wmjo@ewha.ac.kr
J.-S. Park
SKKU Advanced Institute of Nano Technology (SAINT) and Department of Nano Engineering
Sungkyunkwan University
Suwon 16419, Republic of Korea
G. Y. Kim
Advanced Photovoltaics Research Center
Korea Institute of Science and Technology
Seoul 02792, Republic of Korea
W. Jo
New and Renewable Energy Research Center
Ewha Womans University
Seoul 03760, Republic of Korea

The ORCID identification number(s) for the author(s) of this article can be found under https://doi.org/10.1002/aenm.202402117

© 2024 The Author(s). Advanced Energy Materials published by Wiley-VCH GmbH. This is an open access article under the terms of the Creative Commons Attribution-NonCommercial-NoDerivs License, which permits use and distribution in any medium, provided the original work is properly cited, the use is non-commercial and no modifications or adaptations are made.

DOI: 10.1002/aenm.202402117

Herein, we unveil the alterations in both electronic and ionic conduction due to equilibrium space-charge effects under both dark and illuminated conditions at the heterojunction between SnO_2 and $FAPbI_3$, which primarily function as the electron transport layer (ETL) and archetype of extensively researched class of perovskites for the light-harvesting layer in PSCs. The mechanism of spatially inhomogeneous charge distribution initiated by ionic charge adsorption at the oxide transporting layer along the vertical direction across perovskite films are discussed. The dynamics of charge distribution involving ions and electrons are demonstrated through work-function and band bending at the interface via band alignment, along with delicate quantification of charge accumulation dependent on depletion widths. From these findings, we identify that the unbalanced charge distribution is influenced by passivation materials, and the ions absorbed at the interface significantly affect iodide segregation, leading to an increase in iodine vacancies and the volatilization of the FAI. Conversely, the self-assembled 2D perovskite at the embedded NH_4^+-SnO_2/$FAPbI_3$ heterointerface reinforces resistance of iodide oxidation, inhibiting segregation and alleviates the ionic defects. Thus, the charge imbalance induced by iodine vacancies and the accumulation of electronic charges due to ions adsorbed at the interface are addressed.

2. Ionic Adsorption and Emergence of the 2D Phase at the SnO_2/$FAPbI_3$ Heterointerfaces

Based on surface chemistry, either cations or anions are selectively adsorbed onto oxide surfaces, resulting in the accumulation of corresponding vacancies.[16] To regulate the space-charge effects according to the degree of adsorbed ions from oxygen defects, SnO_2 was modified with Cl^- and NH_4^+ on each surface using previous methods,[17] and octylammonium iodide (OAI) was further applied to stabilize the $FAPbI_3$ surface. X-ray photoelectron spectroscopy (XPS) measurements were conducted to verify the ionic adsorption quantity and relative composition to the SnO_2 surface. The detailed preparation of samples is outlined in Figure S1 (Supporting Information). We initially examined the C 1s XPS spectra for ionic absorbed SnO_2 surface (**Figure 1a–c**). As the intensity of the C 1s peak was modulated by varying Sn contents estimated from Sn 3d spectra, the ionic adsorption on the SnO_2 surface can be compared based on the respective areas in different ETLs. We identified four components in the C 1s spectra of perovskite. The components in carbon bonding were assigned as follows: C—C[18–20] (or C—H),[18] C—N[18,19] (OA=$C_8H_{20}N$),[20] and C=O[19] (FA).[18,20] The precise peak positions and corresponding areas for samples without OAI and with OAI treatment are presented in Tables S1 and S2 (Supporting Information), respectively. Only two peaks were observed on the SnO_2 surface without OAI, which corresponded to C—C/C—H and FA (Figure 1d–f, first line). Additionally, a new strong peak at binding energy (BE) ≈286 eV for OA content was assured in the OAI-passivated samples (Figure 1d–f, second line). Despite the results pointing to the SnO_2 surface with peeled-off perovskite films, the presence of OA is notable. These findings affirm that OA^+ and I^- can diffuse to the SnO_2 surface, underscoring the influence of the charged interface at the SnO_2 surface. By analyzing the full-width at half-maximum (FWHM) and the areas of a deconvoluted C 1s peak, it was confirmed that OA diffuses more to Cl^--SnO_2 than to SnO_2 and NH_4^+-SnO_2 in the OAI-treated samples. The detailed explanation for the preference of OA adsorption onto the Cl^--SnO_2 surface over other samples will be discussed in the section 4. The peak in the spectra of all samples at ≈288 eV can be attributed to the C=O bond, indicating the presence of FA ions on the SnO_2 surface. Without OAI, the corresponding areas of the FA peak decrease, and the FWHM increases when comparing with the passivated samples of Cl^- and NH_4^+ with SnO_2. This suggests that FA can be more absorbed on the SnO_2 surface. After the OAI passivation on the perovskite surface, the absorbed FA contents on the SnO_2 surface are more prominently present compared to the conditions without OAI. However, a notable reduction in the C—C/C—H peak, located approximately at 284 eV, was verified and attributed to the mitigation of common surface contamination typically encountered in samples prepared ex situ.[21] This is because of the treatment with 2-propanol (C_3H_8O, IPA), a widely employed solvent for dissolving organic ammonium salts such as OAI and anchoring to process it to the perovskite surface during treatment,[22] as well as for cleaning organic contamination. Moreover, π-π bonding arose on the SnO_2 surface at ≈292 eV[19] after treatment with NH_4^+.

The SnO_2 surface manifests representative intrinsic defects, V_O and OH^-.[23] Hence, we anticipated that the adsorption of ions on the SnO_2 surface could be influenced by the surface defects (OH^- and V_O) of SnO_2 due to their electrical forces. To demonstrate the presence of Pb^{2+} and I^-, which are representative adsorptive ions on the SnO_2 surface affected by OH^- and V_O on different ETLs, we derived the ratio of OH^- to V_O from the normalized O 1s XPS spectra (Figure S2, Supporting Information). Additionally, we conducted a comparison between the Pb^{2+}/Sn and I^-/Sn ratios concerning different ETLs by analyzing the Pb 4f and I 3d spectra (Figure S3, Supporting Information). This correlation is distinctly visible in Figure 1g,i. In the results where OAI was absents (Figure 1g), the presence of OH^- occupied a larger proportion than V_O in Cl^-- and NH_4^+-SnO_2, as opposed to the SnO_2 films alone. The V_O and OH^- reduction occurs by mediating Cl^- and NH_4^+. After OAI treatment on the perovskite surface, the ratio of OH^- components was larger than V_O for all samples (Figure 1i). Compared to the results for Pb^{2+} and I^-, it was shown that larger proportions of OH^- induce Pb^{2+} adsorption on the SnO_2 surface, while larger portions of V_O induce I^- adsorption (Figure 1h,j). These findings align with the O 1s results, indicating induced charges on the SnO_2 surface due to V_O and OH^-. Additionally, passivation effects are evident through the reduction in the presence of Pb and I on Cl^-- and NH_4^+-SnO_2. The remaining Pb and I in Cl^--SnO_2 are lower than in NH_4^+-SnO_2 without OAI (Figure 1h); however, the results with the OAI treatment show the opposite trend (Figure 1j). This is attributed to the 2D phase at the NH_4^+-SnO_2-based heterojunction with OAI, preventing the adsorption of additional ions. As a result of OAI passivation, the charged interface undergoes a transformation from the positive charge of Pb^{2+} to the negative charge of I^- in the Cl^- and NH_4^+-treated samples. The reduction in the quantity of OH^- on SnO_2, as compared to V_O, as determined from the fitting of the normalized O 1s deconvoluted data, is evident in Figure 1j. The elevated FA^+ on SnO_2 is suggested by a greater abundance of absorbed I^- compared to Pb^{2+}.

For further investigation of chemisorbed ETLs, steady-state PL experiment was conducted. The 2D-OA_2PbI_4[19] phase is

© 2024 The Author(s). Advanced Energy Materials published by Wiley-VCH GmbH

16146840, 2024, 40, Downloaded from https://onlinelibrary.wiley.com/doi/10.1002/aenm.202402117 by Ewha Womans University Library, Wiley Online Library on [16/01/2025]. See the Terms and Conditions (https://onlinelibrary.wiley.com/terms-and-conditions) on Wiley Online Library for rules of use; OA articles are governed by the applicable Creative Commons License

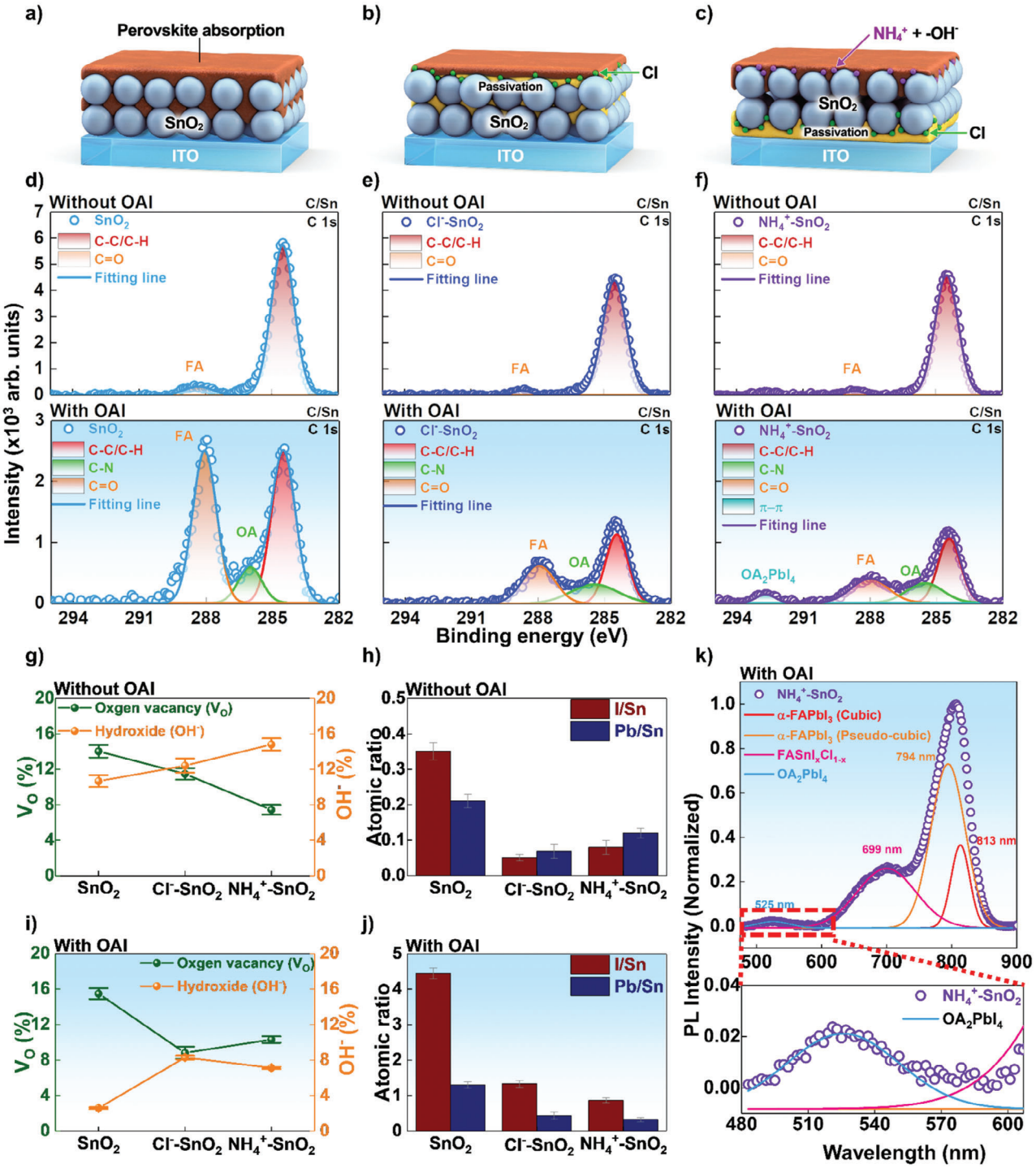


Figure 1. Atomistic state on the SnO_2 surface with peeled-off perovskite thin film. a–c) A schematic illustration depicting perovskite absorption on the SnO_2 surface, contrasting between a) SnO_2 without ETL passivation and b) Cl^--SnO_2 and c) NH_4^+-SnO_2 with ETL passivation. d–f) Comparison of the degree of ionic adsorption to the SnO_2 surface. C 1s XPS spectra illustrating the chemisorbed SnO_2 surface without (in the first line) and OAI (in the second line with a gradational sky-blue color in the graph) on perovskite films, specifically for d) SnO_2, e) Cl^--SnO_2, and f) NH_4^+-SnO_2. To compare the area of ion adsorption, C 1s spectra were characterized by the Sn ratio derived from Sn 3d peaks. g,i), The quantification of oxygen vacancies (V_O) and hydroxide (OH^-) was determined by analyzing the normalized O 1s peak of the chemisorbed SnO_2 surface. h,j) The residual Pb^{2+} and I^- are derived from the atomic ratio for the Sn content on the chemisorbed SnO_2 surface. The error bars in the XPS results were derived from a statistical analysis conducted on data obtained from five distinct samples. k) Photoluminescence (PL) results for the perovskite peeled-off NH_4^+-SnO_2 surface. The 2D phase of the OA_2PbI_4 peak is observed near 525 nm. The emissions in 2D are enlarged under the whole graph. Each data point is representative of three samples. The graph highlights the results of perovskite treated with OAI with a gradational sky-blue color. XPS and PL measurements of chemisorbed ETLs were repeated multiple times to minimize experimental error.

© 2024 The Author(s). Advanced Energy Materials published by Wiley-VCH GmbH

16146840, 2024, 40, Downloaded from https://onlinelibrary.wiley.com/doi/10.1002/aenm.202402117 by Ewha Womans University Library, Wiley Online Library on [16/01/2025]. See the Terms and Conditions (https://onlinelibrary.wiley.com/terms-and-conditions) on Wiley Online Library for rules of use; OA articles are governed by the applicable Creative Commons License

observed to form on the NH_4^+-SnO_2 surface in samples treated with OAI, a phenomenon corroborated by steady-state PL analysis, as depicted in Figure 1k. Compared to other ETLs, a distinctive 2D peak was detected on the NH_4^+-SnO_2 surface in OAI-treated samples, which is notably pronounced (Figure S4, Supporting Information). The diffusion of OAI from the top surface to the buried interface was identified using time-of-flight secondary ion mass spectrometry (ToF-SIMS) depth profiling. Additionally, the self-assembled 2D-OA_2PbI_4 at the buried interface was directly confirmed by high-resolution transmission electron microscopy (HR-TEM), providing direct evidence of the 2D phase formation. These multiple verifications strongly indicate the 2D phase at the buried interface of the OAI-treated NH_4^+-SnO_2 sample and will be comprehensively discussed in Section 4.

3. Assessment of Space Charge Region's Impact on Electronic and Ionic Charge Dynamics

Comprehending the electronic and ionic charge behavior at the heterointerface between the transporting layer and perovskite is crucial, as it directly governs device performance, which is influenced by the uniformity of the charge distribution within the perovskite layer. **Figure 2** presents the results of charge-carrier dynamics and band diagram at the negatively charged interface due to I^- adsorption on the OAI-treated perovskite interface, as initially illustrated in Figure 1, utilizing the I 3d XPS findings. Following OAI passivation atop the $FAPbI_3$ surface, the presence of diffused OA^+ and I^- on the SnO_2 surface was confirmed. Consequently, a higher adsorption of ionic charges was generated at the interface in samples treated with OAI compared to their counterparts without OAI. The anticipated alteration of representative charge-carrier conductivities and concentration defined as iodine vacancies ($V_I^{\bullet}$), conduction band electrons ($e^{'}$), and valence band holes ($h^{\bullet}$),[6,16] is depicted in Figure 2a–f. The $V_I^{\bullet}$ defect constitutes the ionic majority carriers, being a component of ionic conductivity (σ_{ion}) in halide perovskites such as $MAPbI_3$, $FAPbI_3$, $CsPbI_3$, and so on.[3,16] $FAPbI_3$ exhibits n-type properties, with $e^{'}$ and $h^{\bullet}$ as electronic majority and minority charge carriers, respectively, constituting of electronic conductivities (σ_{eon}). The interfacial adsorption of ions causes accumulation and depletion of electronic and ionic charges, thereby creating a rebuilt SCR at the SnO_2/$FAPbI_3$ heterointerfaces.

To verify the interface effects, we conducted parallel conductance measurements determining σ_{eon} and σ_{ion}. These measurements were performed using galvanostatic DC polarization, wherein we evaluated the thickness dependence of $FAPbI_3$ films on various ETLs coated onto Au-patterned electrodes[6,16] (Note S1 and Figure S5, Supporting Information). Subsequently, we plotted the normalized electronic and ionic sheet conductance ($Y_{eon}^{||}$(L) and $Y_{ion}^{||}$(L)) as a function of thickness (L) using polarization data collected at each L point (Figure 2g–i; Note S2, Supporting Information). In contrast to the results without OAI (Figure S6 and Note S3, Supporting Information), reduced ionic conduction is observed in all of the films, despite the higher adsorption of ionic charges at the interface. This suggests that the OAI capping layer obstructs halide segregation under biased field conditions, both in the dark and illuminated states (detailed in Figure S19, Supporting Information). Typically, ionic and electronic charge accumulation, resulting from the displacement of $V_I^{\bullet}$ and $h^{\bullet}$, is facilitated at the negatively charged interface (Figure 2g,h). However, in the NH_4^+-treated SnO_2 interface passivated with the self-assembled 2D perovskite (Figure 2i) although it has a negatively charged interface, the fitting results indicate both electronic and ionic depletion results. To elucidate the effects of 2D perovskite, the energy band diagram was analyzed, as depicted in Figure 2j–l, showing band bending supported by UPS results (Figures S7 and S8, Supporting Information), alongside the degree of accumulation and depletion width obtained from DC polarization results dependent on perovskite thickness coated on different ETLs, contingent upon the presence of OAI. We measured the energy levels of three regions, which indicate the top surface of the $FAPbI_3$ films, interface (ETL/$FAPbI_3$ heterointerface, see Figure S9, Supporting Information), and the chemisorbed SnO_2 surface. Although we expected a greater accumulation of electronic and ionic charge at the interface in SnO_2 (Figure 2j) compared to Cl^--SnO_2 (Figure 2k) due to the significant adsorption of I^-, the measured values of both $\Delta Y_{ion}^{||}$ and $\Delta Y_{eon}^{||}$ (electronic excess charge conductance, Table S3, Supporting Information) for SnO_2 and Cl^--SnO_2 indicate opposite results, with higher contributions of both $h^{\bullet}$ and ionic accumulation in Cl^--SnO_2. Because electrons are the majority carriers in n-type perovskite films, the accumulation and depletion effects are generally influenced by electrons rather than holes. However, an inversion regime from n-type to p-type manifested at the Cl^--SnO_2 interface due to the greater accumulation of holes. This phenomenon is assumed to arise from the built-in space charge on the Cl^--SnO_2 side, which is predominantly ionically dominated by Cl^- as a passivator, resulting in the generation of potential energy disparity. To assess the energy imbalance within the perovskite films, the difference in values between the interface ($|E_{CBM}\text{-}E_F|_{interface}$) and the top surface ($|E_{CBM}\text{-}E_F|_{top\text{-}surface}$) was confirmed by applying UPS results (Table S4, Supporting Information). A larger discrepancy indicates a heightened level of imbalance. On the contrary, NH_4^+-SnO_2 (Figure 2l) exhibits a reduction of $V_I^{\bullet}$, $h^{\bullet}$, and $e^{'}$ at the interface, showing low energy disparity within perovskite films. Specifically, the depletion of electronic charge contributes to the depletion of $h^{\bullet}$ rather than $e^{'}$, leading to a uniform distribution of the majority carrier $e^{'}$ and a lowering of work function compared to the top surface. There is a downward band bending effect, leading to a lowered work function at the interface rather than on the top surface, thereby facilitating electron transfer and maintaining the charge balance across the film. At the NH_4^+-SnO_2 interface, the self-assembled 2D-OA_2PbI_4 is expected to inhibit ionic charge accumulation, reduce $V_I^{\bullet}$, and promote uniform electronic charge distribution throughout the out-of-plane direction of the perovskite films. Both OAI-treated perovskite top surface and chemisorbed ETLs exhibit lower work function values compared to their counterparts without OAI treatment. Interestingly, we observed that the work function values at the interface of SnO_2 and Cl^--SnO_2 based devices are higher than those at the top surface. However, in the case of the NH_4^+-SnO_2 interface, which features the formation of the self-assembled 2D-OA_2PbI_4, the work function (4.8 eV) is lower than the value at the top surface (4.85 eV). A reduction in $|E_{CBM}\text{-}E_F|$ within the chemisorbed ETLs was confirmed, while an increase was validated at the top surface. This energy level alignment is favorable for efficient electron extraction at the ETL/perovskite

© 2024 The Author(s). Advanced Energy Materials published by Wiley-VCH GmbH

16146840, 2024, 40, Downloaded from https://onlinelibrary.wiley.com/doi/10.1002/aenm.202402117 by Ewha Womans University Library, Wiley Online Library on [16/01/2025]. See the Terms and Conditions (https://onlinelibrary.wiley.com/terms-and-conditions) on Wiley Online Library for rules of use; OA articles are governed by the applicable Creative Commons License

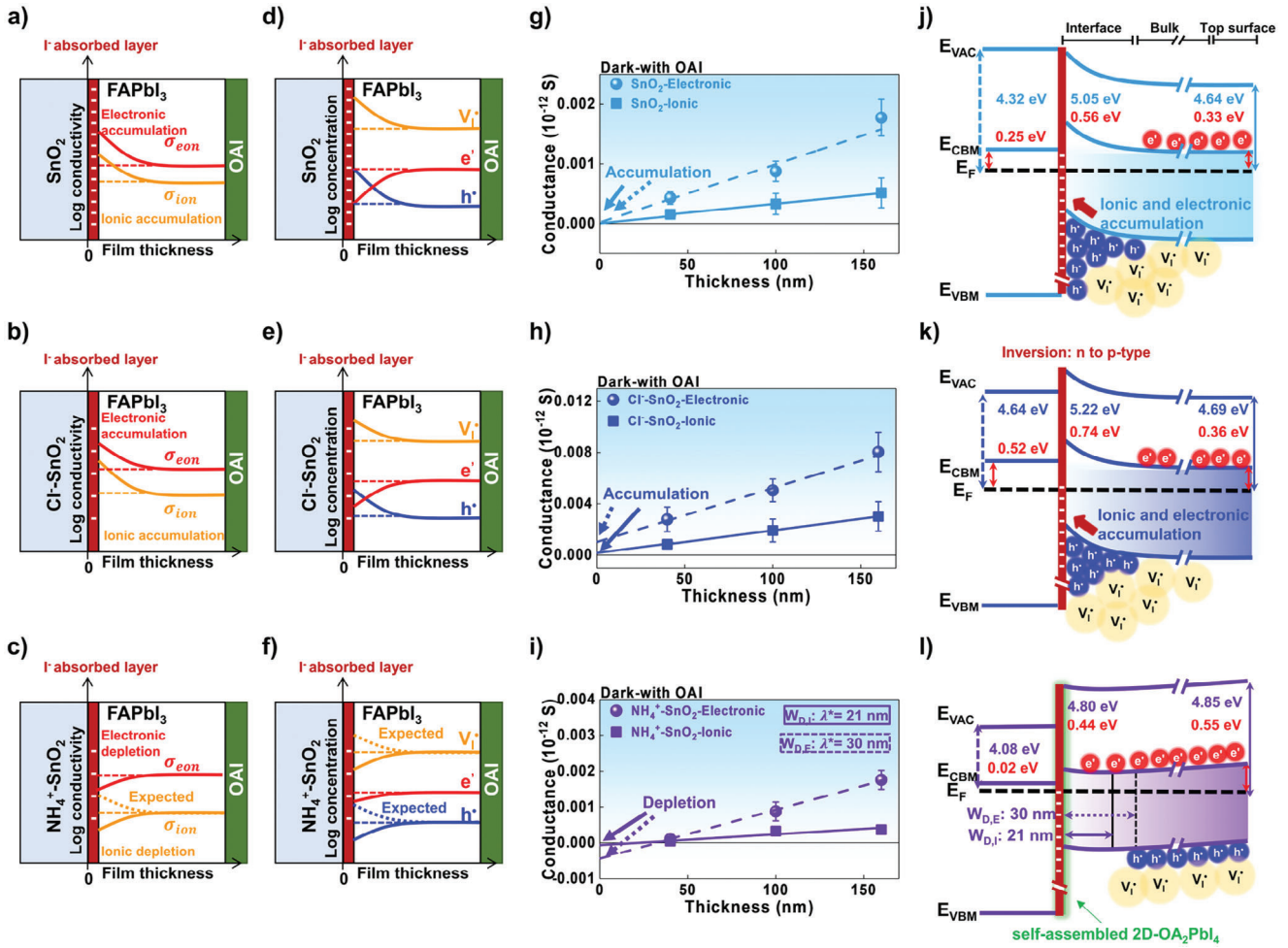


Figure 2. Schematic illustrating charge-carrier behaviors and band diagrams at SnO_2/$FAPbI_3$ heterointerfaces. a–c) Schematic alterations resulted from DC polarization measurement in ionic and electronic conductivities between $FAPbI_3$ and charged layer, composed of absorbed I^-, on SnO_2. The regulation of interfacial accumulation and depletion is governed by the charged interface. d–f) Schematic for the expected behavior of ionic ($V_I^{\bullet}$) and electronic conductor concentrations (e', and $h^{\bullet}$) at SnO_2/$FAPbI_3$ heterointerfaces. g–i) Plots of the normalized electron and ion sheet conductance ($Y_{eon}^{||}$ and $Y_{ion}^{||}$) versus $FAPbI_3$ thickness (L) measured through the DC polarization measurement. This measurement supports the results of electronic and ionic conductivities. j–l) Band diagrams of $FAPbI_3$ on various ETLs, which were constructed by measuring energy levels using ultra-violet photoelectron spectroscopy (UPS) and electronic and ionic space charge regions (SCRs) ($W_{D,E}$, and $W_{D,I}$) obtained from DC polarization measurement. The E_{VAC}, E_{CBM}, E_F, and E_V represent the energy levels of the vacuum level, conduction band minimum (CBM), Fermi level, and valence band maximum (VBM). The work function values ($|E_{VAC}$-$E_F|$) for chemisorbed ETLs, interface, and top surface of the perovskite were indicated in sky-blue, blue, and purple colors, respectively, near their corresponding regions. The energy level difference between E_{CBM} and E_F ($|E_{CBM}$-$E_F|$), representing the degree of hole and electron concentrations, was marked in red on the band diagram. The band bending at the interface is attributed to the unaltered Fermi level caused by the absence of transverse current flow from $FAPbI_3$ to SnO_2 in the lateral device. The first, second and third lines correspond to the results of SnO_2, Cl^--SnO_2, and NH_4^+-SnO_2, respectively.

interface and hole extraction at the perovskite/HTL interface in NH_4^+-SnO_2 based devices. Furthermore, the reduction in the work function of NH_4^+-SnO_2 leads to an increase in the built-in potential (V_{bi}), as illustrated in **Figure 3**f. Enhanced V_{bi} is expected to promote charge separation and collection within the device. Notably, the device performance was enhanced after OAI treatment for all samples. These results will be thoroughly discussed in Figure 3.

The photo-effect on chemical diffusion coefficient (D^{δ}), resistance (R^{δ}), and capacitance (C^{δ}) for the OAI-treated perovskite films according to ETLs at the interface (40 nm) and top surface (300 nm) was investigated (Note S4 and Figure S10, Supporting Information). The value of D^{δ} was determined from the time constant of the transients of DC polarization fitting curves. During illumination, the electronic conductivity prevails over its ionic counterpart within the SnO_2/$FAPbI_3$ heterostructures. Given that electrons constitute the majority carriers rather than holes, the behaviors of electrons predominantly dictate the values of D^{δ}, R^{δ}, and C^{δ}. The trends in diffusion coefficients across all samples exhibit consistency across thicknesses of 40 and 300 nm. Notably, NH_4^+-SnO_2 demonstrates the lowest chemical capacitance values across all scenarios, characterized by low R^{δ} under illuminated conditions and high R^{δ} under dark conditions.

© 2024 The Author(s). Advanced Energy Materials published by Wiley-VCH GmbH

16146840, 2024, 40, Downloaded from https://onlinelibrary.wiley.com/doi/10.1002/aenm.202402117 by Ewha Womans University Library, Wiley Online Library on [16/01/2025]. See the Terms and Conditions (https://onlinelibrary.wiley.com/terms-and-conditions) on Wiley Online Library for rules of use; OA articles are governed by the applicable Creative Commons License

To ascertain interfacial effects on the surface morphologies and crystal properties of perovskite films, we conducted field-emission scanning electron microscopy (FE-SEM) as depicted in Figure S11 (Supporting Information) and X-ray diffraction (XRD) measurements, as illustrated in Figure S12 (Supporting Information). The grain size of $FAPbI_3$ films based on Cl^--SnO_2 and NH_4^+-SnO_2 exhibited a slight increase compared to their counterparts based on SnO_2, as evidenced by the FE-SEM image. Furthermore, the crystalline phase of $FAPbI_3$ films based on NH_4^+-SnO_2 was enhanced, with the observed hexagonal phase of $FAPbI_3$ (δ-$FAPbI_3$)[24] at $2\theta = 11.7°$ of SnO_2 and Cl^--SnO_2 disappearing in the XRD pattern results of NH_4^+-SnO_2. The interface effect mechanism can be attributed to the residual NH_4^+ ions present after the substitution of the OA^+ cation in the OA_2PbI_4 perovskite (Figure S30, Supporting Information). These remaining NH_4^+ ions diffuse within the $FAPbI_3$ films and occupy defect states, such as FA^+ cation vacancies. This process helps inhibit the formation of iodine vacancies, which have a weak binding energy with the metal cation Pb^{2+}. By occupying these defect states, the NH_4^+ ions hinder phase distortion and the generation of the δ-phase, which is a photo-inactive perovskite phase. Consequently, this leads to an improvement in the crystallinity of the perovskite film. Moreover, the reduction of iodine vacancies within the $FAPbI_3$ films due to the presence of NH_4^+-SnO_2 was confirmed by the lower ionic conductivities observed in Figure 2 of the manuscript. This finding supports the proposed mechanism of enhanced crystallinity in the perovskite films through the interfacial effects.

4. Correlation between Iodide Segregation with Charge Transport under Illuminated Conditions

We constructed PSCs consisting of ITO/SnO_2/$FAPbI_3$/OAI/Spiro-OMeTAD/Au, incorporating various ETLs such as SnO_2, Cl^--SnO_2, and NH_4^+-SnO_2 and evaluated the power conversion efficiency (PCE) of each device as shown in Figure 3a–c. The output of the best cell performance treated with OAI for all samples is shown in Table S5 (Supporting Information). The PSCs with NH_4^+-SnO_2 demonstrated superior performance among various ETL-based PSCs incorporating OAI (Figure 3c). Specifically, the top-performing NH_4^+-SnO_2 PSC achieved a PCE of 24.38% in reverse scan and 23.78% in forward scan. The steady-state output efficiencies, measured with pre-stabilized samples, were 21.01% for SnO_2 (Figure 3a), 19.50% for Cl^--SnO_2 (Figure 3b), and 24.31% for NH_4^+-SnO_2 (Figure 3c), each corresponding to a maximum voltage recorded at 1.01, 0.910, and 1.04 V, respectively. Both SnO_2 and Cl^--SnO_2 PSCs exhibit a short-term stability decrease of 6.74%, reaching 93.26%, while NH_4^+-SnO_2 maintains

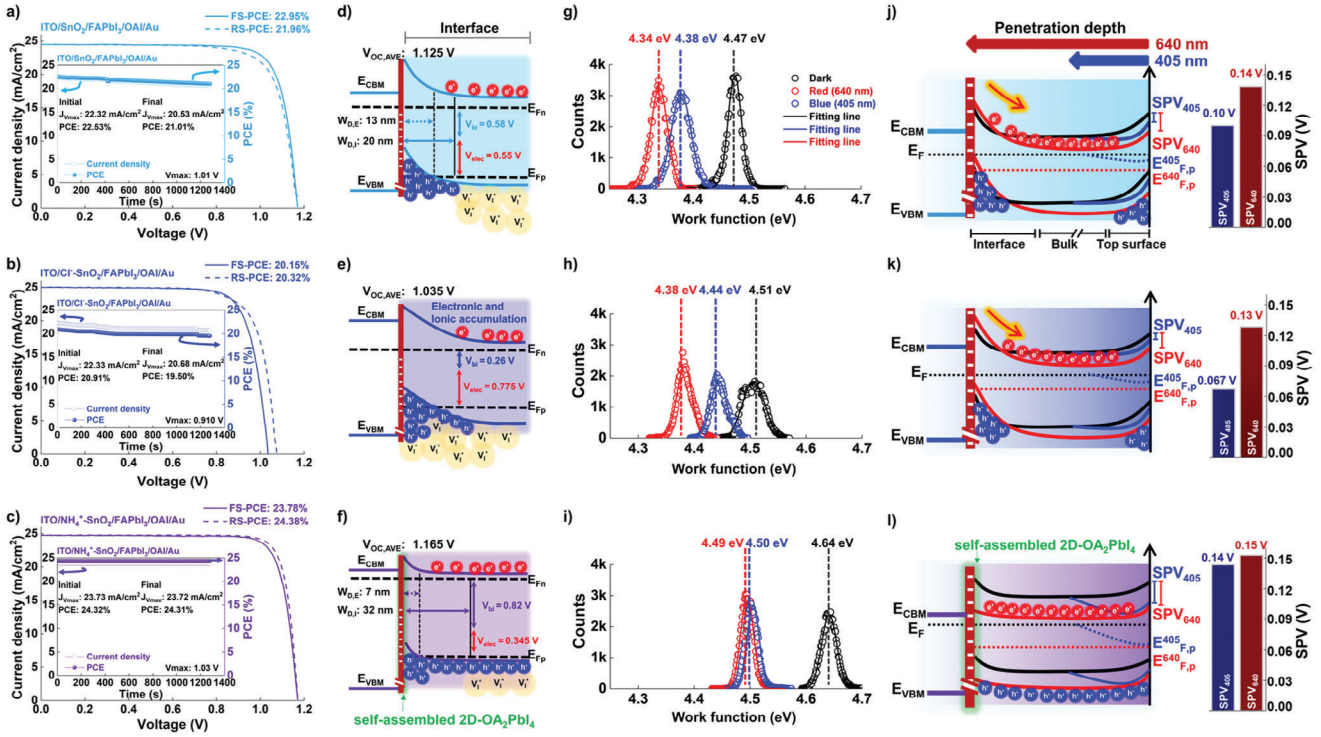


Figure 3. Optoelectronic device performance and characteristics of OAI-treated perovskite. a–c) Representative current density - voltage (*J*–*V*) curves for the best-performing PSCs are presented, together with an inset image displaying the steady-state power output at the maximum power point during 1276 s. d–f) Interface band diagrams at the steady-state system extracted from the normalized electronic and ionic conductance plots as a function of $FAPbI_3$ thickness dependent on the different ETLs under 1 mW cm^{-2} illumination by using a 532 nm laser. The measurement was executed with a perovskite thickness of 40, 100, and 160 nm. The electronic charges, represented by red spheres for electrons and blue spheres for holes, as well as ionic charges such as $V_I^{\bullet}$ are depicted within the band diagram. g–i) Work function values under dark and illuminated conditions were obtained by transforming SPV at 640 and 405 nm using Kelvin probe force microscopy (KPFM). j-l) Corresponding band diagrams were constructed based on the surface photo-voltage (SPV) results (right side), delineating the embedded interface adjacent to the SnO_2 layers with space charges, the bulk, and the surface. The first, second and third data correspond to the results of SnO_2, Cl^--SnO_2, and NH_4^+-SnO_2, respectively.

© 2024 The Author(s). Advanced Energy Materials published by Wiley-VCH GmbH

16146840, 2024, 40, Downloaded from https://onlinelibrary.wiley.com/doi/10.1002/aenm.202402117 by Ewha Womans University Library, Wiley Online Library on [16/01/2025]. See the Terms and Conditions (https://onlinelibrary.wiley.com/terms-and-conditions) on Wiley Online Library for rules of use; OA articles are governed by the applicable Creative Commons License

a high stability of 99.96%. For all samples, average photovoltaic parameters were compared and derived from statistical chart (Figures S13 and S14, and Tables S6 and S7, Supporting Information). The performance of device was further evaluated through external quantum efficiency (EQE) measurements (Figure S15, Supporting Information). The short-circuit current density (J_{SC}) for all samples consistently exhibited values in the range of 24–25 mA cm^{-2}, aligning with the integrated J_{SC} values obtained from the EQE measurements. We achieved a remarkable enhancement of the fill factor by 84%; the fill factor is affected by charge carrier extraction at the interface.[25] In order to probe the electronic charge extraction dynamics at the SnO_2/$FAPbI_3$ interface and recombination rates at the top surface of $FAPbI_3$, we executed measurements involving steady-state PL and time-resolved PL (TRPL) at both the anterior and posterior surfaces of the Glass/ETL/$FAPbI_3$/OAI structure (Figure S16, Supporting Information). We used an excitation laser with a 405 nm wavelength in this measurment and the penetration depth for perovskite films was ≈100 nm (Figure S17, Supporting Information). The excitation from the front and back sides, along with the penetration depth, corresponds to the response of carrier dynamics at the top surface and interface, respectively. The SnO_2 interface exhibited prominent electronic and ionic charge accumulation, whereas the NH_4^+-SnO_2 based PSCs demonstrated a more homogeneous charge distribution. The charge accumulation at the SnO_2 interface hinders the efficient extraction of electrons from the perovskite to the ETL. Notably, in NH_4^+-SnO_2, the top surface exhibited the most prominent PL peak and the longest carrier lifetime, while the interface displayed the lowest PL peak and the shortest carrier lifetime among all samples (Table S8, Supporting Information). These findings underscore an improved capacity for charge carrier extraction at the interface and a reduction in non-radiative recombination on the top surface of $FAPbI_3$. The enhancement is attributed to the reduction in both ionic and hole accumulation and the formation of well-aligned band structure, facilitated by the self-assembled 2D-OA_2PbI_4 at the NH_4^+-SnO_2/$FAPbI_3$ interface. The open-circuit voltage (V_{OC}) of Cl^--SnO_2 is primarily reduced from 1.125 ± 0.018 V (averaged reference cell with SnO_2) to 1.035 ± 0.020 V, indicating an increase in non-radiative recombination on the top surface of $FAPbI_3$ and a decrease in carrier transport capability at the interface, as supported by both steady-sate PL and TRPL results.

In the open-circuit (OC) state, electron-hole pairs are generated under light illumination, leading to the splitting of the quasi-Fermi levels for electrons (E_{Fn}) and holes (E_{Fp}), respectively.[26] The E_{Fn} and E_{Fp} are located near the E_{CBM} and E_{VBM}, respectively. The V_{OC} is predominantly influenced by the difference in the spliting Fermi levels within the perovskite films and related to the internal recombination and work function of the charge-transporting contacts.[26,27] It has been suggested that charge accumulation is one of the main effects of the increase in V_{OC}.[28] Ronen Gottesman et al.[28] demonstrated that photovoltage is influenced by the V_{bi} as well as an additional electrostatic potential (V_{elec}), which is generated by the accumulation of a minority carrier's at the (quasi) Fermi level of the ETL/perovskite interface. The formed total photovoltage is given by $V_{OC} = V_{bi} + V_{elec}$. To further explore the variations in V_{OC} associated with the interface in PSCs, we analyzed the properties of SnO_2/$FAPbI_3$ heterointerface at the steady-state condition from thickness-dependent conductance measurements under light illumination through DC polarization (Figure S18, Supporting Information). The charge dynamics, including both accumulation and depletion effects, as well as the energy band bending at the interface, were analyzed. The $W_{D,E}$ and $W_{I,E}$ were employed to describe these phenomena, along with band diagram under OC state illustrated in Figure 3d–f. The V_{OC} was determined using the mean values from each statistical distribution dataset, and the V_{bi} was computed based on the difference in work function among the ETL, measured values, and HTL, with the latter as reference data (4.9 eV).[29] The V_{elec} was calculated by using $V_{elec} = |V_{OC} - V_{bi}|$. As V_{elec} increases, V_{OC} tends to decrease because V_{bi} decreases proportionally to the charge accumulated at the interface, resulting in lower extraction efficiency. Notably, all samples exhibited upward band bending during illumination, attributed to hole accumulation at the negatively charged interface. In addition, depletion effects characterized by a decrease in $W_{D,E}$ and an increase in $W_{D,I}$ are observed in SnO_2 and NH_4^+-SnO_2, despite accumulation effects observed for SnO_2 under dark conditions. These observations suggested that the oxide particles significantly reduce the lifetime of photo-generated electronic carriers.[16] However, in Cl^--SnO_2, electronic and ionic accumulation is observed despite these changes. These results demonstrate that the V_{oc} of Cl^--SnO_2 was compensated through hole accumulation, contrary to the least effect observed in NH_4^+-SnO_2. Furthermore, we can estimate that significant accumulation and decreased $W_{D,I}$ of $V_I^\bullet$ are attributed to the iodide segregation under illuminated conditions. At the 2D-perovskite self-passivated interface, resistance to the easy oxidation of iodide has been shown under illuminated condtions through increased $W_{D,I}$ and reduction of $\sigma_{ion,\,light}$ in comparison to greatly enhanced $\sigma_{eon,\,light}$ (Figure S19, Supporting Information). To investigate the behavior of electronic and ionic charge, at the interface dominated by the SCR, under both dark and illuminated conditions, we contrasted the electronic bulk conductivities obtained from the slope ($\sigma_{interface}$) of thickness-dependent conductance results with those obtained from the 300 nm (1 м) thickness of perovskite bulk ($\sigma_{surface}$) (Figure S19 and Tables S9 and S10, Supporting Information). The $\sigma_{interface}$ is influenced by space-charge at the interface, while the $\sigma_{surface}$ is primarily affected by the surface rather than the interface, owing to 100 nm penetration depth of the 532 nm green laser source. The total conductivities (σ_{tot}), described in Figure S20 (Supporting Information), are calculated as the sum of $\sigma_{interface}$ (baby-pink) + $\sigma_{surface}$ (sky-blue). Overall, the interface effects perceived in OAI-treated surpass those of samples without OAI treatment, resulting in an increase in σ_{tot}. The enhanced device performance with OAI treatment, specifically NH_4^+-SnO_2 with 2D-perovskite, can be attributed to rise of $\sigma_{surface}$ affected by interface effects and the reduction of $\sigma_{ion,\,light}$ by increasing resistance to iodide oxidation. In the OAI-treated Cl^--SnO_2, the $\sigma_{surface}$ is less than $\sigma_{interface}$, indicating that the dominant effect arises from electronic and ionic charge accumulation at the SCRs.

Light induced iodide segregation and generation of $V_I^\bullet$ begin at the buried interface, and the behavior of $V_I^\bullet$ near the SCR affects the $\sigma_{eon,\,light}$ value, which is related to the device output. Under illumination conditions, we hypothesized that photogenerated charge carriers would be significantly influenced by the SCRs within the perovskite structure. To discern the motion of

© 2024 The Author(s). Advanced Energy Materials published by Wiley-VCH GmbH

16146840, 2024, 40, Downloaded from https://onlinelibrary.wiley.com/doi/10.1002/aenm.202402117 by Ewha Womans University Library, Wiley Online Library on [16/01/2025]. See the Terms and Conditions (https://onlinelibrary.wiley.com/terms-and-conditions) on Wiley Online Library for rules of use; OA articles are governed by the applicable Creative Commons License

electronic carriers across the perovskite films, influenced by the behavior of ionic carriers at the SCRs under illumination, we conducted additional experiments focusing on the spatial distribution of charge carriers across various regions (interface, bulk, and top surface), including the SCR. We used SPV measurements, which measure the light-induced change in the surface potential, assisted by KPFM method.[30] SPV enables the examination of the SCR when the adsorption length of photons is sufficient to generate an excess of free carriers in deeper regions, as the potential of the free surface is linked to any other illuminated region.[31] The perovskite film, with a thickness of 300 nm (1 м), underwent an in-depth investigation of the SCR using a 640 nm laser with a penetration depth of 300 nm, enabling analysis across the entire film thickness. Additionally, a 405 nm laser with a shallower penetration depth of 100 nm, facilitating examination of the bulk and top surface regions. In Figure 3g–i, the work function distribution of OAI-treated perovskite films was converted from contact potential difference ($V_{CPD} = \frac{\Phi_{tip} - \Phi_{perovskite\ films}}{-e}$, Φ_{tip}: work function of metal tip, Φ_{tip}: work function of the perovskite films) measured by KPFM (Figure S21, Supporting Information) in different ETLs under dark ($V_{CPD,\ Dark}$) and illuminated ($V_{CPD,\ Illumination}$) conditions (405 and 640 nm). SPV values indicates that difference between V_{CPD} under dark and illuminated conditions (SPV = $|V_{CPD,\ Illumination} - V_{CPD,\ Dark}|$). The magnitude of SPV indicates the efficiency of the charge seperation with less non-radiative recombinaton. Figure 3j–l presents corresponding band diagrams for all regions (interface, bulk, and top surface), elucidating SPV values by depicting the charge accumulation effects of band bending at the interface and top surface. The disparity between SPV values at 640 nm (SPV_{640}) and SPV values at 405 nm (SPV_{405}) arises from interface charge accumulation. This disparity is attributed to the differential charge distribution across the perovskite film, correlating with the respective laser penetration depths. Typically, we observed higher SPV values for the red laser compared to the blue laser. This phenomenon can be explained by the presence of a negatively charged interface, which induces a preferential migration of excited electrons toward the perovskite bulk and top surface. The opposite results were confirmed without-OAI samples which have positively charged interface (Figure S23, Supporting Information). Concurrently, this charge redistribution leads to hole accumulation at the interface. The cumulative effect manifests as a reduction in the illuminated work function values and a contraction of depletion widths at the top surface relative to dark conditions. In the SPV_{640} results for SnO_2 and Cl^--SnO_2, the accumulation of holes at the interface pulls electrons to the top surface, leading to an increase in SPV_{640} at the surface compared to SPV_{405}. Consequently, the SPV_{640} value surpasses the SPV_{405}. Conversely, the SPV_{640} and SPV_{405} values are nearly identical in NH_4^+-SnO_2, indicating a uniform electronic charge distribution across all regions. Furthermore, our analysis indicates that the blue SPV is particularly sensitive to surface defects. Lower blue SPV values are indicative of a high concentration of defect states on the perovskite surface, likely due to enhanced non-radiative recombination processes. The interpretation of SPV values can be linked to voltage loss phenomena associated with charge recombination and non-radiative processes.[32,33] SPV_{640} values are more suitable for analyzing the voltage loss of samples compared to their SPV_{405} counterparts, as SPV_{640} considers the charge distribution across the entire region of the perovskite films. NH_4^+-SnO_2 exhibits the highest SPV_{640} among the ETLs, consistent with the higher V_{OC} observed for NH_4^+-SnO_2. Additionally, separate investigations without OAI samples further verified our results (Figures S22 and S23, Supporting Information). In an illuminated state, the movement of electronic charges is significantly more sensitive to SCRs than in dark conditions. Importantly, our results demonstrate the efficacy of 2D perovskite passivation in mitigating both surface and bulk defects. This passivation strategy appears to facilitate a more homogeneous charge distribution across the perovskite films under light-illuminated conditions, potentially enhancing the overall optoelectronic performance of the material.

5. Impact of Ionic Migration Barriers and Adsorbed Species on Interfacial Phase Distortion

Spatial distribution of ionic charge in the out-of-plane of $FAPbI_3$ films, ToF-SIMS depth profiles were executed for structures without and with OAI passivation (ITO/ETL/$FAPbI_3$ and ITO/ETL/$FAPbI_3$/OAI) based on various ETLs (Figure S24, Supporting Information). The ions evaluated as representatives include OA^+ ($C_8H_{20}N^+$) and Sn^+ with OAI samples for positive polarity, and I^-, Cl^-, and SnO_2^- for negative polarity. In our previous study,[17] XPS analysis of the ETL/ITO structure did not detect residual Cl^- ions in either SnO_2 or NH_4^+-SnO_2 samples, in contrast to Cl^--SnO_2. The presence of Cl^- originates from the MACl additive incorporated into the $FAPbI_3$ precursor solution.[34] While most Cl^- in perovskite films evaporated during the annealing,[35] residual Cl^- bonded with SnO_2 due to V_O of surface. The higher concentration of residual Cl^- at the buried interface of SnO_2 compared to NH_4^+-SnO_2 is attributed to surface defect states in SnO_2 films. In NH_4^+-SnO_2 films, fewer V_O are present, and residual Cl^- evaporates due to reaction with Cl^- and NH_4^+ at the interface, forming HCl gas. Thus, residual Cl^- components are reduced on NH_4^+-SnO_2 surfaces. Besides, the OA^+ can diffuse from the top surface to the buried interface and the amounts of OA^+ diffusion exhibited an increase proportional to the Cl^- concentration at the interface across all OAI-treated samples. Specifically, the elevated OA^+ concentration at the Cl^--SnO_2 interface compared to other samples, was consistent with the C 1s XPS findings (Figure 1). This phenomenon potentially indicates the preferential bonding of diffused OA^+ with Cl^- rather than I^-. To validate this, Figure S25 (Supporting Information) presents density functional theory (DFT) calculations of the stabilized bonding length between OAI and OACl. The findings reveal that the stability of the OACl + I combination is 1.01 eV higher than that of OAI + Cl, underscoring OA's preference for binding with Cl rather than I. Thus, we can infer that the predominant combinations of ions or molecules occupying the buried interface are OAI + I^- for SnO_2, OACl + I^- for Cl^--SnO_2, and 2D-OA_2PbI_4 for NH_4^+-SnO_2. Based on these analyses, the distribution of ionic and electronic charges within the vertical direction of OAI-treated perovskite is elucidated as illustrated in **Figure 4a**.

Formation of OACl bonding at the buried interface of Cl^--SnO_2 leaves I^-, which readily bonds with FA and generates FAI (g). The volatilization of FAI (g) produces accumulation of $V_I^{\bullet}$

© 2024 The Author(s). Advanced Energy Materials published by Wiley-VCH GmbH

16146840, 2024, 40, Downloaded from https://onlinelibrary.wiley.com/doi/10.1002/aenm.202402117 by Ewha Womans University Library, Wiley Online Library on [16/01/2025]. See the Terms and Conditions (https://onlinelibrary.wiley.com/terms-and-conditions) on Wiley Online Library for rules of use; OA articles are governed by the applicable Creative Commons License

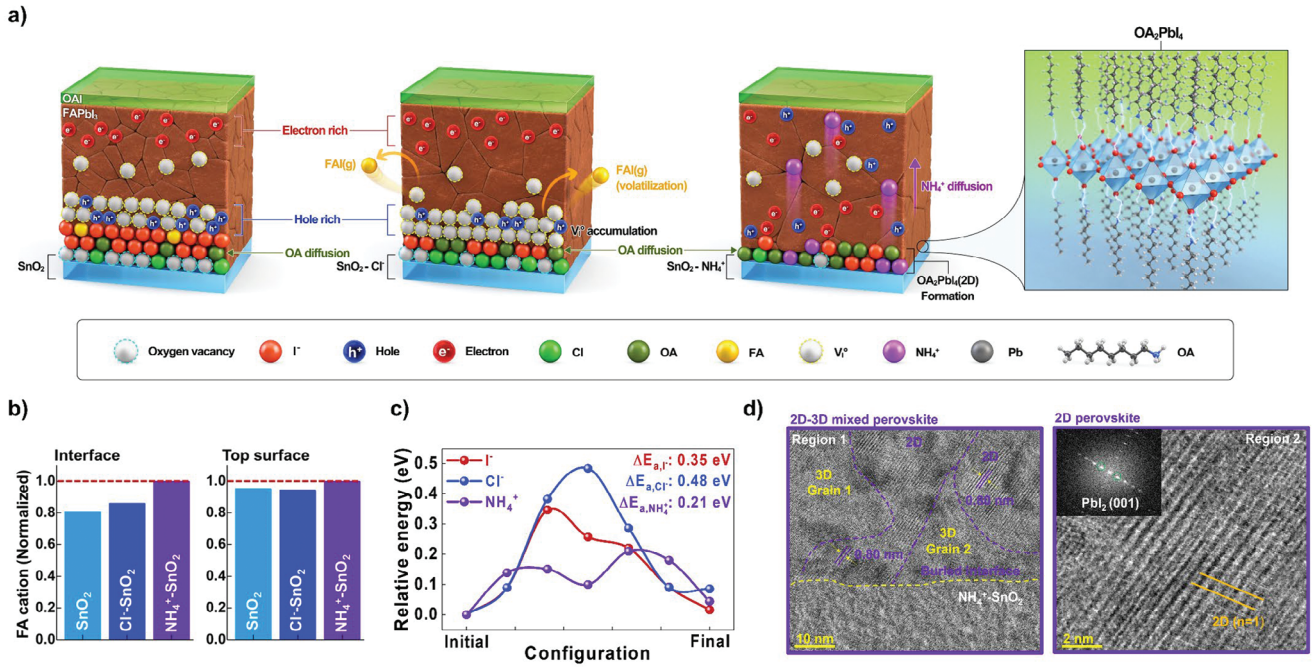


Figure 4. Charge distribution and ionic dynamics at perovskite interfaces with different ETLs. a) Illustration of electronic and ionic transport within $FAPbI_3$ on different ETLs. The self-assembled 2D-OA_2PbI_4 is indicated at the NH_4^+-SnO_2/$FAPbI_3$ heterointerface. b) Quantities of FA cations determined by analyzing the atomic ratio of XPS N 1s spectra at various thicknesses of the perovskite films. c) Ion migration transition and barrier energies of I^-, Cl^-, and NH_4^+ in $FAPbI_3$. d) Cross-sectional HR-TEM images of the NH_4^+-SnO_2/$FAPbI_3$ buried interface. The full area is shown in Figure S31 (Supporting Information) along with other ETLs.

at the interface, as demonstrated in Figure 2j. To scrutinize the relationship between OACl bonding and FAI volatilization, and the increased generation of $V_I^\bullet$, XPS analysis was employed to compare the amounts of FA cations in OAI/$FAPbI_3$ films based on the ETLs at both 20 nm (interface) and 600 nm (top surface) thicknesses of the perovskite layer (Figure 4b). From the N 1s spectra of the $FAPbI_3$ films, two main peaks correspond to the FA cation (≈400 eV) and OA cation (≈402 eV).[36] The quantities of FA cations were acquired by the ratio of the FA/Pb with reference to the OA (Figure S26, Supporting Information). The measurements were executed across five distinct samples to augment precision, with error bars depicted on the bar graph. At the top surface (600 nm), where the influence of the interface is minimal, the concentration of FA cations remains nearly consistent across all samples. In the 20 nm thickness, where space-charge effects generated by absorbed ions on SnO_2 are more pronounced at the interface compared to the 600 nm thickness, the quantities of FA cations were diminished both at the Cl^--SnO_2 and the SnO_2 rather than NH_4^+-SnO_2. The amounts of I anions at the buried interface were further estimated by using cross-sectional scanning transmission electron microscopy (STEM) and energy dispersive X-ray spectroscopy (EDS) for the ITO/SnO_2/$FAPbI_3$/OAI/Spiro structure as illustrated in Figure S27 (Supporting Information). The detected atoms are I and In, representing $FAPbI_3$ and the substrate of ITO, respectively. Gradual reduction in I anions occurs as the $FAPbI_3$ films approach the buried interface compared to the top surface, particularly evident in the case of SnO_2 and Cl^--SnO_2, unlike NH_4^+-SnO_2. These discoveries support the results of $V_I^\bullet$ accumulation in DC polarization and substantiates the notion that Cl^-, when bound with OA^+, contributes to the depletion of FAI. The robustness of the bond between OA^+ and Cl^- exceeds that of OAI, facilitating the subsequent bonding of I^- with FA^+. Consequently, the FAI can readily evaporate at the Cl^--SnO_2/$FAPbI_3$ interface. The evaporation of FAI is particularly notable due to the presence of Cl^- as the passivation material, which enhances the grain size and crystallinity of the perovskite films.

For a more in-depth investigation into the cause of bulk inhomogeneity concerning the absorbed ions at the interface, we conducted a comparison of the migration barrier (ΔE_a)[37] of remaining ions, including I^-, Cl^-, and NH_4^+, in $FAPbI_3$. This analysis was performed through DFT calculations (Figure 4c), utilizing the atomic structure of $FAPbI_3$ ($FA_8Pb_8I_{24}$) as illustrated in Figure S28 (Supporting Information). To avoid an unnatural alignment in a single direction during the calculation, efforts were made to orientate them in as diverse directions as possible. The relative energy corresponding the diffusion of ions was calculated through from the initial to the final configuration for $FAPbI_3$ bonded with I^-, Cl^-, and NH_4^+. The complete diffusion process of NH_4^+ and Cl^- in the $FAPbI_3$ configurations is illustrated in Figure S29 (Supporting Information). Among the calculated ions (I^-, Cl^-, and NH_4^+), we determined that the migration barrier of NH_4^+ ($\Delta E_{a,NH_4^+}$) exhibits the lowest barrier energy, being 0.21 eV, lower than that of I^- ($\Delta E_{a,I^-}$) and Cl^- ($\Delta E_{a,Cl^-}$). The Cl^- and I^- anions show higher ΔE_a than the NH_4^+, in the case

© 2024 The Author(s). Advanced Energy Materials published by Wiley-VCH GmbH

16146840, 2024, 40, Downloaded from https://onlinelibrary.wiley.com/doi/10.1002/aenm.202402117 by Ewha Womans University Library, Wiley Online Library on [16/01/2025]. See the Terms and Conditions (https://onlinelibrary.wiley.com/terms-and-conditions) on Wiley Online Library for rules of use; OA articles are governed by the applicable Creative Commons License

of I^-, it is more mobile than Cl^-, similar to previous results.[37] When ions with high ΔE_a values remain at the ETL interface, alterations in space-charge effects, which induce the accumulation or depletion of excess charges, can occur, resulting in unexpected charge behaviors across the films. With the diffusion of OA cations toward the interface, coupled with the remarkably low $\Delta E_{a,NH_4^+}$, and the emergence of metaphase NH_4PbI_3 at the NH_4^+-SnO_2/$FAPbI_3$ interface, NH_4^+ can be substituted by OA, precipitating to the formation of 2D-OA_2PbI_4 (Figure S30, Supporting Information). After the synthesis of 2D-OA_2PbI_4, the remaining NH_4^+ ions migrate into the $FAPbI_3$ films and occupy defects related to FA^+ and Pb^{2+}. This process brings about the aforementioned alteration of work function, resulting in well-aligned band-bending both at the interface and the top surface, ultimately leading to the production of high-quality films. NH_4^+-SnO_2, showing minimal interfacial adsorption of halide anions such as I^- and Cl^-, and forming 2D-OA_2PbI_4 at the interface, demonstrates a uniform charge distribution within the bulk (Figure 4a).

Space-charges at the interface, causes non-uniformity in charges along the out-of-plane directions, ultimately influencing the perovskite lattice distortion,[38,39] including altering the Pb—I bonding length through variations in the crystal structure. Therefore, it is essential to systematically investigate the structural variations resulting from the accumulation of ions at the buried interface. The vertical charge homogeneity of the perovskite films was evaluated through the analysis of cross-sectional HR-TEM images for the structure of ITO/ETL/$FAPbI_3$/OAI (Figure 4d; Figure S31, Supporting Information) and ITO/ETL/$FAPbI_3$/OAI/HTL/Au (Figure S32, Supporting Information). Notably, we observed the self-assembled 2D-OA_2PbI_4 (n = 1) near the NH_4^+-SnO_2 interface, which was incorporated into the 3D perovskite structure (Figure S31a, Supporting Information). This 2D perovskite formation occurred between the 3D perovskite structures, resulting in a 2D-3D mixed perovskite phase at the buried interface. As a result of OA^+ cation diffusion process and subsequent reaction with the existing metaphase NH_4PbI_3 structure, a mixed 2D-3D perovskite phase emerged, particularly concentrated near the NH_4^+-SnO_2 buried interface. The interplanar spacing of the 2D-OA_2PbI_4 lattice for the PbI_2 (001) plane was measured at 0.8 nm, exceeding that of typical 3D perovskite structures due to the large size of the OA^+ cation. In contrast, other buried interfaces showed no evidence of 2D perovskite formation (Figure S31b,c, Supporting Information). Further, we detected amorphous phases near the SnO_2 interface, which could potentially serve as fast decomposition routes for PSCs due to rapid absorption of water and oxygen.[40]

6. Association between Vertical Film Strain and Long-Term Operational Stability of Devices

Distinct regions within vertical perovskite films, including the interface, bulk, and top surface, were segmented to gather information on the interplanar spacing of the lattice (d) and explore potential phase distortions.[25] The analysis of representative $d_{PbI_2(001)}$ and $\alpha(111)$ ($d_{(111)}$) domains was carried out, accompanied by their corresponding fast Fourier transform (FFT) images. Additionally, the normal distribution of all d-spacing in a bar graph, along with the standard deviation, is presented in **Figure 5a–c**. The d-spacing in the PbI_2 (001) domains exhibits a pronounced decrease along the vertical direction, from the interface to the top surface, in the case of SnO_2 and Cl^--SnO_2. Conversely, NH_4^+-SnO_2 demonstrates a more gradual decrease in interplanar spacings. In the NH_4^+-SnO_2, the interplanar spacings values of 0.667 and 0.360 nm align well with PbI_2 (001) and $\alpha(111)$ domains, respectively for $FAPbI_3$.[18] In Cl^--SnO_2, $d_{(111)}$ is significantly reduced, whereas $d_{PbI_2(001)}$ is larger than the well-agreed values of NH_4^+-SnO_2. However, $d_{(111)}$and $d_{PbI_2(001)}$ of SnO_2 are larger than their counterparts for NH_4^+-SnO_2. The increase in $d_{PbI_2(001)}$ and $d_{(111)}$ of SnO_2 can be attributed to the elongation of the Pb-I bond length, influenced by the presence of V_O on the surface of SnO_2.[36] In the scenario involving Cl^--SnO_2, the introduction of Cl^- at the interface elicits a displacement of the Pb atom, resulting in an elongation of the Pb-I bond length as evidenced by the outcomes of DFT analysis. To assess the vertical inhomogeneity with residual-strain of the perovskite thin films induced by SCRs at the interface, reflecting lattice mismatch, we investigated the space charge induced stress distribution in vertically oriented $FAPbI_3$ films on the various ETLs (Figure 5d–f). The stress analysis utilized depth-dependent grazing incident X-ray diffraction (GIXRD), which combined classical $\sin^2\varphi$ measurements to examine the in-plane residual strain.[41] The representative out of plane depths are interface (500 nm), bulk (200 nm), and top surface (50 nm). The diffraction data were meticulously analyzed at consistent depths, employing the Gaussian distribution function. Intriguingly, as the penetration depth decreased, a consistent downward shift in peak position toward lower 2θ values was observed, as detailed equipment angles in Table S11 (Supporting Information) and visually depicted in Figure S33 (Supporting Information). Generally, $\sin^2\varphi$ and 2θ follow a linear relationship and the slope of the fitting line stands for the magnitude of the residual stress $\sigma = -\frac{E}{2(1+\nu)}\frac{\pi}{180^\circ}cot\theta_0\frac{\partial(2\theta)}{\partial\sin^2\varphi}$ where E is the perovskite modulus, ν is Poisson's ratio of the perovskite, where E and ν were evaluated as 11.45 GPa, 0.3, respectively.[41,42] The regression lines of SnO_2 (Figure 5d) and Cl^--SnO_2 (Figure 5e) revealed negative slopes with downward peak shifting unlike NH_4^+-SnO_2 (Figure 5f), indicating an enlargement of the (100) crystal planes as they extend toward the out-of-plane direction at the same probed depth[41] (Table S12, Supporting Information). This suggests that both SnO_2 and Cl^--SnO_2, which were shown greater electronic and ionic accumulation rather than NH_4^+-SnO_2, experiences tensile strain due to io space-charge induced stress at the interface.

To evaluate the correlation between tensile strain and stability of the PSCs with a stabilized buried interface achieved through the self-assembled 2D-OA_2PbI_4, demonstrating a high efficiency, we conducted a long-term operational stability test and aging test following ISOS protocol.[43] Unencapsulated PSCs were tested under various conditions: ambient storage at room temperature with 35–45% RH for 2070 h (ISOS-D-1), high humidity aging at 70–75% RH, and thermal stress for 360 h at 65 °C (ISOS-D-2I) (Figure 5g). The thermal stress test was conducted inside a nitrogen-filled glovebox to control humidity and oxygen levels, isolating the effect of heat. Results show that Cl^--SnO_2 based PSCs exhibit comparable thermal stability to NH_4^+-SnO_2 based devices, despite having greater tensile strain in the film. The

© 2024 The Author(s). Advanced Energy Materials published by Wiley-VCH GmbH

16146840, 2024, 40, Downloaded from https://onlinelibrary.wiley.com/doi/10.1002/aenm.202402117 by Ewha Womans University Library, Wiley Online Library on [16/01/2025]. See the Terms and Conditions (https://onlinelibrary.wiley.com/terms-and-conditions) on Wiley Online Library for rules of use; OA articles are governed by the applicable Creative Commons License

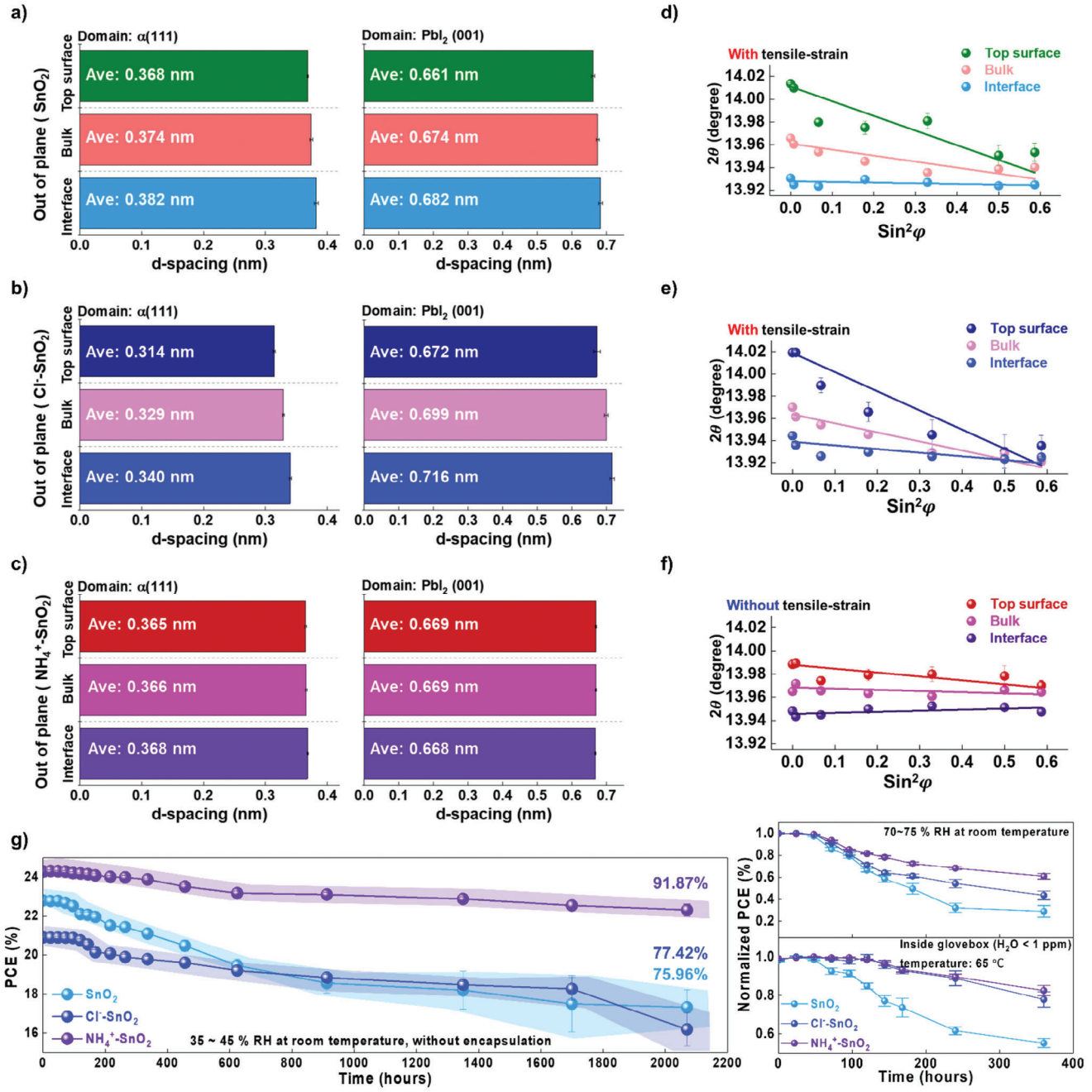


Figure 5. Vertical structural analysis and operational stability assessment of perovskite films. a–c) Interplanar lattice spacing for the out of plane direction of OAI-treated $FAPbI_3$ on the various ETLs. Statistics of various d-spacing at each lattice were extracted from FFT pattern images (Figure S32, Supporting Information) of HR-TEM results and are presented as statistical bar charts. d-f) Space charge induced residual strain distribution was analyzed using depth-dependent diffraction data, which were linear fits of 2θ-$\sin^2\varphi$ from $\psi = 0^\circ$ to $\psi = 50^\circ$ for perovskite films deposited on d) SnO_2, e) Cl^--SnO_2, and f) NH_4^+-SnO_2 ETLs. g) Long-term operational stability of PSCs was assessed by storing them at a relative humidity (RH) of around 35–45% and room temperature for 2070 h. Additionally, the devices were subjected to stress under RH exceeding 70–75%. The thermal stability of devices was evaluated when stressed at 65 °C in a nitrogen-filled glovebox (30 ppm < H_2O and 1 ppm < O_2). All devices were in an un-encapsulated state. For each stability test condition, a statistically significant sample of 18–20 devices was evaluated.

thermal stability of PSCs is more strongly correlated with the concentration of oxygen defects (such as V_O and OH^-) present in high concentrations on SnO_2 films, rather than with film strain. As observed in TEM results, Cl^- at the buried interface increased Pb-I bonding length, while the (111) plane spacing decreased, indicating a compressed perovskite structure. Although the increased Pb-I bond length suggests potentially higher $V_I^\bullet$ concentration, thermal stress for Cl^- based PSCs appears to densify the structure, inhibiting ion migration and interfacial reactions, thus enhancing thermal stability. This densification effect may

© 2024 The Author(s). Advanced Energy Materials published by Wiley-VCH GmbH

16146840, 2024, 40, Downloaded from https://onlinelibrary.wiley.com/doi/10.1002/aenm.202402117 by Ewha Womans University Library, Wiley Online Library on [16/01/2025]. See the Terms and Conditions (https://onlinelibrary.wiley.com/terms-and-conditions) on Wiley Online Library for rules of use; OA articles are governed by the applicable Creative Commons License

explain the unexpected stability despite the initial tensile strain. Furthermore, as evidenced by the TEM images (Figure S31, Supporting Information), amorphous phases were detected at the SnO_2 buried interface. These phases resulted in an increased δ-phase of perovskite and consequently accelerated the degradation of PSCs. It implies that managing oxygen defects could be more crucial for improving PSC stability than addressing film strain. After 2070 h, the NH_4^+-SnO_2 device maintained 91.87% of its initial PCE. The degradation trends in all PSCs correlate with the extent of FAI volatilization, which induces lattice distortion due to presence of oxygen defects and Cl^- at the buried interface. Initial device performance is primarily determined by band-bending at the interface and film homogeneity, while long-term stability depends on structural factors that influence FAI volatilization, potentially impacted by space-charge effects at the interface.

7. Conclusion

Modulation of the SCR at the SnO_2/$FAPbI_3$ heterointerfaces has been shown to depend on the application of passivation, both at the top and the interface. Based on the presence of residual interfacial materials at the SCR, it has been revealed that the interface experiences an accumulation of both electronic and ionic charges, primarily driven by Cl^- and I^- ions, which possess significantly higher migration barriers compared to NH_4^+. Moreover, the elevated migration barrier prompts the volatilization of FAI at the buried interface, resulting in an imbalance of electronic and ionic charges within the perovskite films. Specifically, the formation of OACl bonding, facilitated by the diffusion of OA^+ from the perovskite top surface passivation to the Cl^--dominant interface, fosters the generation of volatilized FAI, thereby exacerbating the charge imbalance. The vertical inhomogeneity of $FAPbI_3$ was ameliorated through the introduction of NH_4^+, characterized by its low migration barrier of 0.21 eV. This species, readily substitutable with diffused OA^+ from top surface of perovskite, consequently, promotes the emergence of the self-assembled 2D-OA_2PbI_4 within the SCR. Through modified SCRs that deplete ionic charges reinforcing resistance iodide oxidation under illuminated conditions and ensure homogeneous electronic charge distribution, the capacity of charge transport across the overall films brought about an impressive fill-factor, with the best-performing PSCs surpassing 84%. This achievement represents 94% of the theoretical limit (89.5%).[25] These discoveries offer novel insights and perspectives regarding the correlation between migration barriers and the homogeneity of charge distribution.

8. Experimental Section

Materials: Tin (IV) oxide (SnO_2, 15% in H_2O) colloidal dispersion precursor was obtained from Alfa Aesar. Lead iodide (PbI_2) was purchased from Tokyo Chemical industry (TCI). Ammonium chloride (NH_4Cl), 4-tert-bytyl pyridine (tBP), lithium bis(trifluoromethanesulfonyl)imide (Li-TFSI), formamidine acetate (FA acetate) (99%), hydroiodic acid (HI) (57 wt% in H_2O, 99.95%), anhydrous chlorobenzene (99.8%), anhydrous ethyl alcohol (99.8%), anhydrous 2-propanol (IPA, 99.8%), anhydrous N,N-dimethylformamide (DMF, 99.8%), and anhydrous dimethyl sulfoxide (DMSO, 99.9%) were purchased from Sigma-Aldrich. Methylammonium chloride (MACl) and n-Octylammonium iodide (OAI) were purchased from Great Cell Solar. Spiro-OMeTAD was purchased from Lumtec. Ether (99%), acetonitrile (99.9%, for cleaning single crystal), and γ-butyrolactone (GBL, 99.5%) were purchased from Samchun. Glass cleaning alcohol such as acetone and IPA were purchased from OCI.

Synthesis of Formamidinium Iodide and $FAPbI_3$ Single Crystal: Formamidinium iodide (FAI = $HC(NH_2)_2I$), in the form of a white powder, was synthesized by stirring 20 g of FA acetate and gradually adding 40 ml of HI using a magnetic stir bar in a round-bottom flask within an ice bath for over 2 h. The solvent HI was removed by utilizing a rotary evaporator with the vacuum pressure controlled at 65 °C, resulting in the collection of yellow and white-colored precipitates. These precipitates were subsequently cleaned multiple times with ether until the powder turned pure white. The white precipitates were dissolved in ethanol and subjected to recrystallization with the addition of ether. This process was repeated twice. The final FAI powder was dried for 24 h in a vacuum oven. $FAPbI_3$ single crystals were collected by reacting 1.6 M pre-synthesized FAI and 1.6 M PbI_2 in γ-butyrolactone at 110 and 140 °C for 1 h each. The resulting black phase $FAPbI_3$ perovskite single crystals were washed sequentially with acetonitrile and ether, followed by drying at 150 °C for 30 min. The FAI powder and $FAPbI_3$ single crystals were stored in an N_2-filled glovebox for future use.

Device Fabrication: Perovskite precursor solutions were prepared in an N_2-filled glovebox by combining 0.455 g of $FAPbI_3$ single crystal with 29 mg of MACl in 400 µL DMF and 50 µL DMSO. Subsequently, SnO_2 thin films were spin-coated on ITO/glass substrates at 4000 rpm for 30 s with a 150 µL SnO_2 solution, prepared by mixing commercial SnO_2 nanoparticles and deionized water (DI water) in a 1:4 ratio. The ITO/glass substrates were sequentially cleaned by ultrasonication in detergent DI water, acetone and IPA, for 15 min each, before deposition. The spin-coated SnO_2 thin films were annealed at 160 °C for 30 min. The Cl^--SnO_2 and NH_4^+-SnO_2 ETLs were fabricated by SnO_2 passivation with NH_4Cl, as conducted in a previous study.[17] UV ozone treatment was applied to all substrates prior to use, including both Cl^- and NH_4^+-passivated SnO_2 thin films. Perovskite thin films were prepared on the SnO_2 ETL using a one-step spin-coating system at 4000 rpm for 25 s, with an initial acceleration rate 800 rpm for 5 s. 780 µL of ether was dropped between 12 and 14 s after the beginning of spinning. The spin-coated perovskite thin films were sequentially annealed at 110 and 160 °C for 10 min each. After annealing, an OAI solution was dropped onto the perovskite films. The OAI solution was prepared by adding 0.0193 g of OAI to 5 ml of IPA solvent. The HTL was prepared using a spiro-OMeTAD solution, which consisted of 72.3 mg of spiro-OMeTAD powder dissolved in 1 mL of chlorobenzene, along with 30 µL of 4-tert-butylpyridine (tBP) and 35 µL of a lithium bis(trifluoromethanesulfonyl)imide (Li-TFSI) stock solution (260 mg Li-TFSI in 1 mL acetonitrile). The HTL solution was spin-coated onto both the OAI-treated and untreated perovskite films on various ETLs at 3000 rpm for 25 s. Following the coating process, all substrates were placed in a dark desiccator for 1–2 h to enhance doping effects. Subsequently, a 100 nm thick gold electrode was thermally evaporated onto the spiro-OMeTAD film under a vacuum of 5.0×10^{-6} torr using shadow masks.

Solar Cell Characterization: Current density-voltage ($J-V$) data were obtained using a Keithley 4200 source meter under solar simulator illumination (Sol3A Class AAA) calibrated to AM 1.5 G one sun (100 $mW \cdot cm^{-2}$) with reference silicon solar cells (ORIEL SRC-1000-TC-QZ-N). Solar cell ($J-V$) curves were measured from −0.1 to 1.2 V (forward scan) and 1.2 to -0.1 V (reverse scan) at 5 $mV \cdot s^{-1}$ scan rate. During J-V measurements, a device was shielded by a black metal mask with an aperture area of 0.049 cm^2. The external quantum efficiency was measured using a solar cell quantum efficiency test system (McScience K3100 IQX), then normalized over 300–1100 nm, and light source spectral response was calibrated using a silicon detector. Measurements were performed using an Oriel Instrument QEPVSI-b system with Xenon arc lamp (Moden Jay, LP-Xe 300 W) chopped at 30 Hz and monochromator (THORLABS).

Film Characterization: XPS and UPS measurements for the chemisorbed ETLs (surface with peeled off perovskite), interface and top surface of perovskite were performed by using an AXIS Supra instrument equipped with a monochromatic Al ($K\alpha$, λ = 1.5406 Å) source for XPS and He I (21.22 eV) for UPS. The photo-carrier dynamics investigation of

© 2024 The Author(s). Advanced Energy Materials published by Wiley-VCH GmbH

16146840, 2024, 40, Downloaded from https://onlinelibrary.wiley.com/doi/10.1002/aenm.202402117 by Ewha Womans University Library, Wiley Online Library on [16/01/2025]. See the Terms and Conditions (https://onlinelibrary.wiley.com/terms-and-conditions) on Wiley Online Library for rules of use; OA articles are governed by the applicable Creative Commons License

ETLs/$FAPbI_3$ heterointerfaces and chemisorbed ETLs was analyzed by fluorescence steady state and time spectrometer FuoTime 300 (PicoQuant) to obtained PL and TRPL using time correlated single photon counting (TCSPC). The all films were coated on the glass substrates and samples were put on the solid sample holder inside the equipment and illuminated with a 405 nm picosecond laser on front (perovskite surface side) and back side (glass side). The laser beam spot size is estimated almost 600 µm in diameter. To investigate the local crystal phase and formation, samples were milling processed with cross-sections by using a focused ion beam (FIB; Helios G4 model) and analyzed by HR-TEM and EDS. The cross-sectional HR-TEM and STEM were collected using a JEM-ARM200F. Gatan Digital Micrograph v.3.9 and Gatan Microscopy Suite v.3.4.3 were used to analyze the cross-sectional HR-TEM images. The primary source for the ToF-SIMS (model: TOF.SIMS-5) experiment was Bi^+ 30 keV, and the etching source for the depth profile experiment was Cs^+ 1 keV. XRD spectra and depth-dependent residual stress measurements were performed using a D8 Advance.2020 multi-purpose XRD instrument (Bruker) and an Xpert Pro (HR-XRD) with an X-ray tube (Cu Kα, λ = 1.5406 Å), respectively. The aforementioned measurements were performed at the National Center for Inter-university Research Facilities (NCIRF) at Seoul National University. Surface morphologies were examined using field emission scanning electron microscopy (Hitachi SU8220) at the Western Seoul Center of the Korea Basic Science Institute, with a beam power of 20 kV. The thickness of perovskite films was estimated using a Dektak profile system (Bruker, DektakXT). Ultraviolet-visible absorption spectra were recorded using a Lambda 35 spectrometer (PerkinElmer).

Surface and Interface Properties: KPFM measurements were performed using an atomic force microscope (n-Tracer, Nano Focus Inc.) equipped with a Pt/Ir-coated non-contact tip (Nanosensors) at an AC voltage of 1 V to analyze the surface potential distributions and extract the work function of the top surface perovskite films. Furthermore, SPV was characterized via KPFM under illumination utilizing external laser dot modules emitting at 640 nm (red, penetration depth: 330 nm) and 405 nm (blue, penetration depth: 100 nm), intensify of 5 mW cm^{-2}. These measurements were conducted within a N_2-filled glovebox system, where O_2 levels were maintained below 30 ppm and H_2O levels below 0.5 ppm, effectively isolating the setup from the external environment. Flattening, an image editing technique, was not utilized in the acquired KPFM and SPV images.

First-Principles Density Functional Theory Computation: Migration of NH_4^+ molecule and interstitial defects was investigated by performing first-principles density functional theory (DFT) calculations. We used Pesos exchange-correlation functionals[44] and project augmented wave (PAW) method,[45] as implemented in the Vienna Ab Initio Simulation Package (VASP).[46] The energy cutoff for the plane waves was set to 400 eV. Structures were relaxed until the residual force becomes <0.03 eV $Å^{-1}$. Climbing nudged elastic band (cNEB) method was employed to estimate the barrier energy.[47]

Galvanostatic DC Polarization and ac Impedance Measurement: Galvanostatic DC polarization experiments were carried out using a high-impedance electrometer (Keithley model 2634b) to induce voltage changes. These measurements were conducted under both dark and illuminated conditions, with careful control over temperature and atmospheric conditions (using Ar flow). Impedance spectroscopy measurements were performed using an AC impedance spectrometer model 1260A frequency response analyzer (Solartron Analytical). The frequency range was swept from 1 MHz to 0.01 Hz, with an AC voltage of 0.1 V applied.

Supporting Information

Supporting Information is available from the Wiley Online Library or from the author.

Acknowledgements

This study was supported by the Basic Science Research Program of the National Research Foundation of Korea (NRF) funded by the Ministry of Education (NRF-2018R1A6A1A03025340). Additional support was provided by the Technology Development Program for Solving Climate Change through the NRF, funded by the Ministry of Science and ICT (NRF-2022M3J1A1064229). Further support was provided by the NRF funded by the Ministry of Science and ICT (RS-2024-00355905).

Conflict of Interest

The authors declare no conflict of interest.

Data Availability Statement

Research data are not shared.

Keywords

2D perovskite, buried interface, ion migration, passivation, perovskite solar cells

Received: May 15, 2024
Revised: July 1, 2024
Published online: August 4, 2024

[1] J. He, D. Li, H. Liu, J. Xiang, J. Bai, Y. Ren, Z. Wang, M. Xia, X. Yin, L. Yuan, F. Zhang, S. Wang, *Adv. Energy Mater.* **2023**, *13*, 971.
[2] X. Zhang, J. X. Shen, M. E. Turiansky, C. G. Van de Walle, *Nat. Mater.* **2021**, *20*, 971.
[3] G. Y. Kim, A. Senocrate, Y. Wang, D. Moia, J. Maier, *Angew. Chem.* **2021**, *133*, 833.
[4] R. He, W. Wang, Z. Yi, F. Lang, C. Chen, J. Luo, J. Zhu, J. Thiesbrummel, S. Shah, K. Wei, Y. Luo, C. Wang, H. Lai, H. Huang, J. Zhou, B. Zou, X. Yin, S. Ren, X. Hao, L. Wu, J. Zhang, J. Zhang, M. Stolterfoht, F. Fu, W. Tang, D. Zhao, *Nature* **2023**, *618*, 80.
[5] S. Zhou, S. Fu, C. Wang, W. Meng, J. Zhou, Y. Zou, Q. Lin, L. Huang, W. Zhang, G. Zeng, D. Pu, H. Guan, C. Wang, K. Dong, H. Cui, S. Wang, T. Wang, G. Fang, W. Ke, *Nature* **2023**, *624*, 69.
[6] A. Senocrate, I. Moudrakovski, G. Y. Kim, T. Yang, G. Gregori, M. Grätzel, J. Maier, *Angew. Chem.* **2017**, *129*, 7863.
[7] G. Y. Kim, A. Senocrate, T. Y. Yang, G. Gregori, M. Grätzel, J. Maier, *Nat. Mater.* **2018**, *17*, 445.
[8] R. Lin, Y. Wang, Q. Lu, B. Tang, J. Li, H. Gao, Y. Gao, H. Li, C. Ding, J. Wen, P. Wu, C. Liu, S. Zhao, K. Xiao, Z. Liu, C. Ma, Y. Deng, L. Li, F. Fan, H. Tan, *Nature* **2023**, *620*, 994.
[9] J. Zhu, Y. Luo, R. He, C. Chen, Y. Wang, J. Luo, Z. Yi, J. Thiesbrummel, C. Wang, F. Lang, H. Lai, Y. Xu, J. Wang, Z. Zhang, W. Liang, G. Cui, S. Ren, X. Hao, H. Huang, Y. Wang, F. Yao, Q. Lin, L. Wu, J. Zhang, M. Stolterfoht, F. Fu, D. Zhao, *Nat. Energy* **2023**, *8*, 714.
[10] L. Duan, D. Walter, N. Chang, J. Bullock, D. Kang, S. P. Phang, K. Weber, T. White, D. Macdonald, K. Catchpole, H. Shen, *Nat. Rev. Mater.* **2023**, *8*, 261.
[11] N. Yantara, N. Mathews, *Joule* **2024**, *8*, 1239.
[12] J. Liu, E. Aydin, J. Yin, M. De Bastiani, F. H. Isikgor, A. U. Rehman, E. Yengel, E. Ugur, G. T. Harrison, M. Wang, Y. Gao, J. I. Khan, M. Babics, T. G. Allen, A. S. Subbiah, K. Zhu, X. Zheng, W. Yan, F. Xu, M. F. Salvador, O. M. Bakr, T. D. Anthopoulos, M. Lanza, O. F. Mohammed, F. Laquai, S. De Wolf, *Joule* **2021**, *5*, 3169.
[13] R. Wang, T. Huang, J. Xue, J. Tong, K. Zhu, Y. Yang, *Nat. Photonics* **2021**, *15*, 411.
[14] M. Kim, G. H. Kim, T. K. Lee, I. W. Choi, H. W. Choi, Y. Jo, Y. J. Yoon, J. W. Kim, J. Lee, D. Huh, H. Lee, S. K. Kwak, J. Y. Kim, D. S. Kim, *Joule* **2019**, *3*, 2179.

© 2024 The Author(s). Advanced Energy Materials published by Wiley-VCH GmbH

16146840, 2024, 40, Downloaded from https://onlinelibrary.wiley.com/doi/10.1002/aenm.202402117 by Ewha Womans University Library, Wiley Online Library on [16/01/2025]. See the Terms and Conditions (https://onlinelibrary.wiley.com/terms-and-conditions) on Wiley Online Library for rules of use; OA articles are governed by the applicable Creative Commons License

[15] S. Tan, T. Huang, I. Yavuz, R. Wang, T. W. Yoon, M. Xu, Q. Xing, K. Park, D. K. Lee, C. H. Chen, R. Zheng, T. Yoon, Y. Zhao, H. C. Wang, D. Meng, J. Xue, Y. J. Song, X. Pan, N. G. Park, J. W. Lee, Y. Yang, *Nature* **2022**, *605*, 268.
[16] G. Y. Kim, A. Senocrate, D. Moia, J. Maier, *Adv. Funct. Mater.* **2020**, *30*, 2002426.
[17] J. Kim, J. Park, Y. Kim, W. Jo, *Small* **2022**, *18*, 2204173.
[18] B. wook Park, H. W. Kwon, Y. Lee, D. Y. Lee, M. G. Kim, G. Kim, K. jeong Kim, Y. K. Kim, J. Im, T. J. Shin, S. Il Seok, *Nat. Energy* **2021**, *6*, 848.
[19] P. Chen, Y. Bai, S. Wang, M. Lyu, J. H. Yun, L. Wang, *Adv. Funct. Mater.* **2018**, *28*, 1706923.
[20] L. Shen, P. Song, L. Zheng, L. Wang, X. Zhang, K. Liu, Y. Liang, W. Tian, Y. Luo, J. Qiu, C. Tian, L. Xie, Z. Wei, *Adv. Mater.* **2023**, *35*, 2301624.
[21] T. J. Jacobsson, J. P. Correa-Baena, E. Halvani Anaraki, B. Philippe, S. D. Stranks, M. E. F. Bouduban, W. Tress, K. Schenk, J. Teuscher, J. E. Moser, H. Rensmo, A. Hagfeldt, *J. Am. Chem. Soc.* **2016**, *138*, 10331.
[22] S. Tan, T. Huang, I. Yavuz, R. Wang, M. H. Weber, Y. Zhao, M. Abdelsamie, M. E. Liao, H. C. Wang, K. Huynh, K. H. Wei, J. Xue, F. Babbe, M. S. Goorsky, J. W. Lee, C. M. Sutter-Fella, Y. Yang, *J. Am. Chem. Soc.* **2021**, *143*, 6781.
[23] S. U. Lee, H. Park, H. Shin, N. G. Park, *Nanoscale* **2023**, *15*, 5044.
[24] S. U. Lee, S. Y. Kim, J. H. Lee, J. H. Baek, J. W. Lee, H. W. Jang, N. G. Park, *Nano Lett.* **2024**, *24*, 4869.
[25] Z. Liang, Y. Zhang, H. Xu, W. Chen, B. Liu, J. Zhang, H. Zhang, Z. Wang, D. H. Kang, J. Zeng, X. Gao, Q. Wang, H. Hu, H. Zhou, X. Cai, X. Tian, P. Reiss, B. Xu, T. Kirchartz, Z. Xiao, S. Dai, N. G. Park, J. Ye, X. Pan, *Nature* **2023**, *624*, 557.
[26] I. Mora-Seró, *Joule* **2018**, *2*, 585.
[27] S. Ravishankar, S. Gharibzadeh, C. Roldán-Carmona, G. Grancini, Y. Lee, M. Ralaiarisoa, A. M. Asiri, N. Koch, J. Bisquert, M. K. Nazeeruddin, *Joule* **2018**, *2*, 788.
[28] R. Gottesman, P. Lopez-Varo, L. Gouda, J. A. Jimenez-Tejada, J. Hu, S. Tirosh, A. Zaban, J. Bisquert, *Chem* **2016**, *1*, 776.
[29] W. T. Wang, P. Chen, C. H. Chiang, T. F. Guo, C. G. Wu, S. P. Feng, *Adv. Funct. Mater.* **2020**, *30*, 1909755.
[30] H. R. Jung, Y. Cho, W. Jo, *Adv. Opt. Mater.* **2022**, *10*, 2102175.
[31] L. Kronik, Y. Shapira, *Surf. Sci. Rep.* **1999**, *37*, 1.
[32] H. K. Park, Y. Cho, J. Kim, S. Kim, S. Kim, J. Kim, K. J. Yang, D. H. Kim, J. K. Kang, W. Jo, *npj Flex. Electron.* **2022**, *6*, 91.
[33] G. Lim, H. K. Park, W. H. Kim, S. H. Kim, K. J. Yang, J. K. Kang, D. H. Kim, W. Jo, *J. Mater. Chem. A* **2023**, *11*, 25555.
[34] D. H. Kang, S. U. Lee, N. G. Park, *ACS Energy Lett.* **2023**, *8*, 2122.
[35] M. Kim, G.-H. Kim, T. K. Lee, I. W. Choi, H. W. Choi, Y. Jo, Y. J. Yoon, J. W. Kim, J. Lee, D. Huh, *Joule* **2019**, *3*, 2179.
[36] J. H. Lee, S. J. Lee, T. Kim, H. Ahn, G. Y. Jang, K. H. Kim, Y. J. Cho, K. Zhang, J. S. Park, J. H. Park, *Joule* **2023**, *7*, 380.
[37] J. Xu, H. Chen, L. Grater, C. Liu, Y. Yang, S. Teale, A. Maxwell, S. Mahesh, H. Wan, Y. Chang, B. Chen, B. Rehl, S. M. Park, M. G. Kanatzidis, E. H. Sargent, *Nat. Mater.* **2023**, *22*, 1507.
[38] Y. Yuan, J. Huang, *Acc. Chem. Res.* **2016**, *49*, 286.
[39] W. Zhu, S. Wang, X. Zhang, A. Wang, C. Wu, F. Hao, *Small* **2022**, *18*, 2105783.
[40] B. P. Nguyen, J. Kim, H. K. Park, W. Jo, G. Y. Kim, *ACS Appl. Energy Mater.* **2022**, *5*, 7965.
[41] C. Zhu, X. Niu, Y. Fu, N. Li, C. Hu, Y. Chen, X. He, G. Na, P. Liu, H. Zai, Y. Ge, Y. Lu, X. Ke, Y. Bai, S. Yang, P. Chen, Y. Li, M. Sui, L. Zhang, H. Zhou, Q. Chen, *Nat. Commun.* **2019**, *10*, 815.
[42] C. Shi, Q. Song, H. Wang, S. Ma, C. Wang, X. Zhang, J. Dou, T. Song, P. Chen, H. Zhou, Y. Chen, C. Zhu, Y. Bai, Q. Chen, *Adv. Funct. Mater.* **2022**, *32*, 2201193.
[43] M. V. Khenkin, E. A. Katz, A. Abate, G. Bardizza, J. J. Berry, C. Brabec, F. Brunetti, V. Bulović, Q. Burlingame, A. Di Carlo, R. Cheacharoen, Y. B. Cheng, A. Colsmann, S. Cros, K. Domanski, M. Dusza, C. J. Fell, S. R. Forrest, Y. Galagan, D. Di Girolamo, M. Grätzel, A. Hagfeldt, E. von Hauff, H. Hoppe, J. Kettle, H. Köbler, M. S. Leite, S.(F.) Liu, Y. L. Loo, et al., *Nat. Energy* **2020**, *5*, 35.
[44] J. P. Perdew, A. Ruzsinszky, G. I. Csonka, O. A. Vydrov, G. E. Scuseria, L. A. Constantin, X. Zhou, K. Burke, *Phys. Rev. Lett.* **2008**, *100*, 136406.
[45] P. E. Blöchl, *Phys. Rev. B* **1994**, *50*, 17953.
[46] G. Kresse, J. Furthmüller, *Phys. Rev. B – Condens. Matter Mater. Phys.* **1996**, *54*, 11169.
[47] G. Henkelman, B. P. Uberuaga, H. Jónsson, *J. Chem. Phys.* **2000**, *113*, 9901.

© 2024 The Author(s). Advanced Energy Materials published by Wiley-VCH GmbH

16146840, 2024, 40, Downloaded from https://onlinelibrary.wiley.com/doi/10.1002/aenm.202402117 by Ewha Womans University Library, Wiley Online Library on [16/01/2025]. See the Terms and Conditions (https://onlinelibrary.wiley.com/terms-and-conditions) on Wiley Online Library for rules of use; OA articles are governed by the applicable Creative Commons License